Layer-By-Layer Entangled Spin-Orbital Texture of the Topological Surface State in Bi_2Se_3

Z.-H. Zhu,[1] C. N. Veenstra,[1] G. Levy,[1] A. Ubaldini,[2] P. Syers,[3] N. P. Butch,[3] J. Paglione,[3] M. W. Haverkort,[4,5] I. S. Elfimov,[1,5] and A. Damascelli[1,5,*]

[1]*Department of Physics and Astronomy, University of British Columbia, Vancouver, British Columbia V6T 1Z1, Canada*
[2]*Département de Physique de la Matière Condensée, Université de Genève, CH-1211 Genève 4, Switzerland*
[3]*Department of Physics, CNAM, University of Maryland, College Park, Maryland 20742, USA*
[4]*Max Planck Institute for Solid State Research, Heisenbergstraße 1, D-70569 Stuttgart, Germany*
[5]*Quantum Matter Institute, University of British Columbia, Vancouver, British Columbia V6T 1Z4, Canada*

(Received 29 January 2013; published 21 May 2013)

We study Bi_2Se_3 by polarization-dependent angle-resolved photoemission spectroscopy and density-functional theory slab calculations. We find that the surface state Dirac fermions are characterized by a *layer-dependent* entangled spin-orbital texture, which becomes apparent through quantum interference effects. This explains the discrepancy between the spin polarization obtained in spin and angle-resolved photoemission spectroscopy—ranging from 20% to 85%—and the 100% value assumed in phenomenological models. It also suggests a way to probe the intrinsic spin texture of topological insulators, and to continuously manipulate the spin polarization of photoelectrons and photocurrents all the way from 0 to $\pm 100\%$ by an appropriate choice of photon energy, linear polarization, and angle of incidence.

DOI: 10.1103/PhysRevLett.110.216401 PACS numbers: 71.20.−b, 71.10.Pm, 73.20.At, 73.22.Gk

Topological insulators (TIs) define a new state of matter in which strong spin-orbit interaction (SOI) leads to the emergence of a metallic topological surface state (TSS) formed by spin-nondegenerate Dirac fermions [1–6]. To capture the physics of TIs, a spin-momentum locking with 100% spin polarization is usually assumed for the TSS in time-reversal invariant models [3–5]. The successful realization of topological insulating behavior in quantum wells [7,8] and crystalline materials such as Bi_2Se_3 [9–11] brings us closer to the practical implementation of theoretical concepts built upon novel topological properties. However, the large discrepancy in the degree of TSS spin polarization determined for Bi_2Se_3 by spin and angle-resolved photoemission spectroscopy (spin-resolved ARPES)—ranging from 20% to 85% [12–16]—challenges the hypothesis of a 100% spin polarization for real TIs. First-principles density-functional theory (DFT) also indicates that the TSS spin polarization in members of the Bi_2X_3 material family (X = Se, Te) can be substantially reduced from 100% [17,18]. Based on general symmetry arguments, it was shown that the spin polarization direction of photoelectrons in spin-resolved ARPES can be very different from that of the TSS wave function [19]. However, the role played by the intrinsic properties of the TSS wave function in defining the highest spin polarization that could be achieved, for instance in dc and photoinduced electrical currents, has remained elusive.

We report here that the TSS many-layer-deep extension into the material's bulk—in concert with strong SOI—gives rise to a layer-dependent, entangled spin-orbital texture of the Dirac fermions in Bi_2Se_3. A remarkable consequence, specifically exploited in this study, is that one can gain exquisite sensitivity to the internal structure of the TSS wave function, Ψ_{TSS}, via quantum interference effects in ARPES. The spin-orbital texture is captured directly in the linear-polarization dependence of the ARPES intensity maps in momentum space, and can be fully resolved with the aid of *ab initio* DFT slab calculations. This has also major consequences in the interpretation of spin-resolved ARPES results, explicitly solving the puzzle of the TSS spin polarization, and suggesting how 100% spin polarization of photoelectrons and photocurrents can be achieved and manipulated in topological-insulator-based devices by using linearly polarized light.

We start our discussion from the Bi_2Se_3 ARPES results in Fig. 1, measured with σ and π linearly polarized 21.2 eV photons [20,21]. Based on the experimental geometry [Fig. 1(a)] and photoemission selection rules, σ-polarization probes the in-plane p_x and p_y orbitals, whereas π polarization a combination of both in-plane and out-of plane (p_z) orbitals: the 80% overall intensity reduction observed by switching from π to σ polarization indicates that the TSS has a dominant p_z character. As for the evolution of the ARPES intensity around the Dirac cone, in σ polarization [Figs. 1(c)–1(e)] we observe a twofold pattern at both 0.1 and 0.2 eV above the Dirac point (DP), consistent with a previous report [22], although somewhat asymmetric with respect to the $k_y = 0$ plane [see in particular Fig. 1(e)]; this suggests a tangential alignment of the in-plane $p_{x,y}$ orbitals with respect to the Dirac constant-energy contours. Conversely in π polarization [Figs. 1(f)–1(h)] we observe a strongly asymmetric pattern at 0.1 eV above the DP, which evolves into a triangular pattern while still retaining some asymmetry at 0.2 eV above the DP; this is in stark contrast to the uniform distribution of intensity along the Dirac contour expected

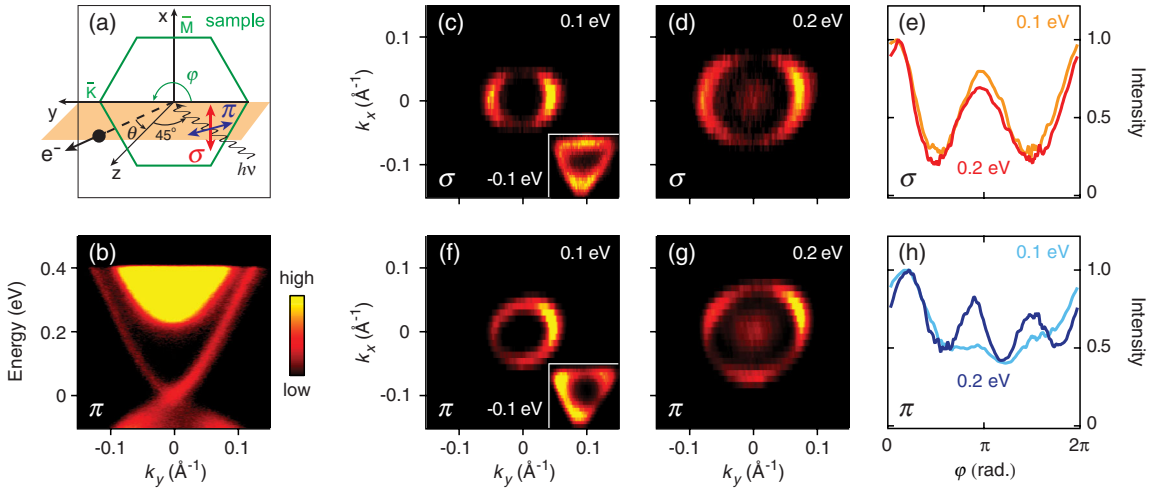

FIG. 1 (color online). (a) Schematics of the experimental geometry, with π (horizontal) and σ (vertical) linear polarizations, and horizontal photoelectron emission plane. (b) ARPES dispersion measured along $\bar{K}-\bar{\Gamma}-\bar{K}$ with π polarization; the zero of energy has been set at the Dirac point (DP) for convenience. (c), (d) Constant energy ARPES maps from above (0.1 and 0.2 eV) and below (-0.1 eV, inset) the DP, measured with σ polarization; (f), (g) same for π polarization. (e), (h) Normalized variation of the σ-(e) and π-polarization (h) ARPES intensity, along the Dirac contours, plotted versus the in-plane angle φ.

for the dominant out-of-plane p_z orbitals. Finally, at -0.1 eV below the DP, a triangular pattern is observed for both polarizations [see insets of Figs. 1(c) and 1(f)].

The asymmetry in ARPES intensity between $\pm\mathbf{k}_{\|}$ is particularly evident in π polarization at 0.1 eV in Fig. 1(f) and in the band dispersion of Fig. 1(b). This finding, which might seem in conflict with the time-reversal invariance of the TSS, provides fundamental clues on the structure of Ψ_{TSS}. Time-reversal invariance requires the state at $+\mathbf{k}$ with (pseudo) spin up to be degenerate with the state at $-\mathbf{k}$ with (pseudo) spin down, i.e., to have the same real-orbital occupation numbers. This so-called Kramers degeneracy, together with the ARPES selection rules for linearly polarized light, forbids intensity patterns which are different at $\pm\mathbf{k}$. We emphasize here that this restriction can be rephrased in terms of purely in-plane momentum coordinates, i.e., $\pm\mathbf{k}_{\|}$, only for a perfect two-dimensional TSS with a delta-function-like density, for which k_z plays no role. Thus the observation of an imbalance in ARPES intensity at $\pm\mathbf{k}_{\|}$, together with the established time-reversal invariance of TIs, necessarily implies that Ψ_{TSS} must have a finite extent, albeit not a dispersion [23], along the third dimension. While details will become clear when discussing our DFT results in Fig. 3, we anticipate that this, together with SOI, leads to a complex layer-dependent spin-orbital entanglement in Bi_2Se_3, which becomes apparent in ARPES through photoelectron interference.

By performing ARPES intensity calculations [20,24] for TSS and bulk wave functions from our DFT slab-calculations, we accurately reproduce the data. As shown in Figs. 2(a)–2(f), we obtain very different intensities at $\pm\mathbf{k}_{\|}$ in excellent agreement with the results for both σ and π polarizations. Specifically, we reproduce the quasi-two-fold pattern in σ polarization, stemming from the spatial configuration of $p_{x,y}$ orbitals [Figs. 2(a) and 2(b)], the quasi-three-fold pattern away from the DP [Fig. 2(e)], which originates from the hybridization between TSS and bulk states [25,26], and also the triangular patterns at -0.1 eV [insets of Figs. 2(a) and 2(d)]. Note that the ARPES intensity visible at the $\bar{\Gamma}$ point in Figs. 1(d) and 1(g), but not reproduced by our calculations, originates from the scattering-induced broadening of the bulk

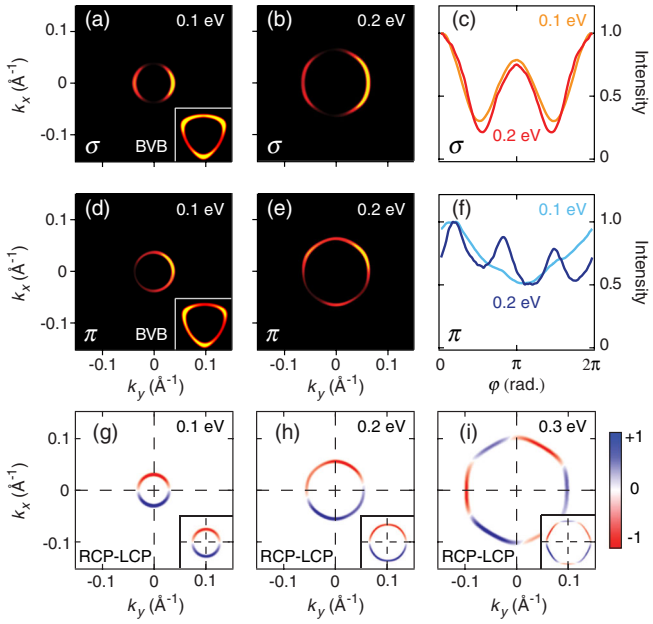

FIG. 2 (color online). (a), (b) Calculated constant-energy σ polarization ARPES maps for TSS (0.1 and 0.2 eV [33]) and bulk valence band (BVB, -0.1 eV in the inset); (c) corresponding variation of the ARPES intensity versus the in-plane angle φ. (d)–(f) Same data as in (a)–(c), but now for π polarization. (g)–(i) Calculated constant-energy circular dichroism ARPES patterns at 0.1, 0.2, and 0.3 eV above the DP; insets: patterns obtained by rotating the sample by 90° about the normal.

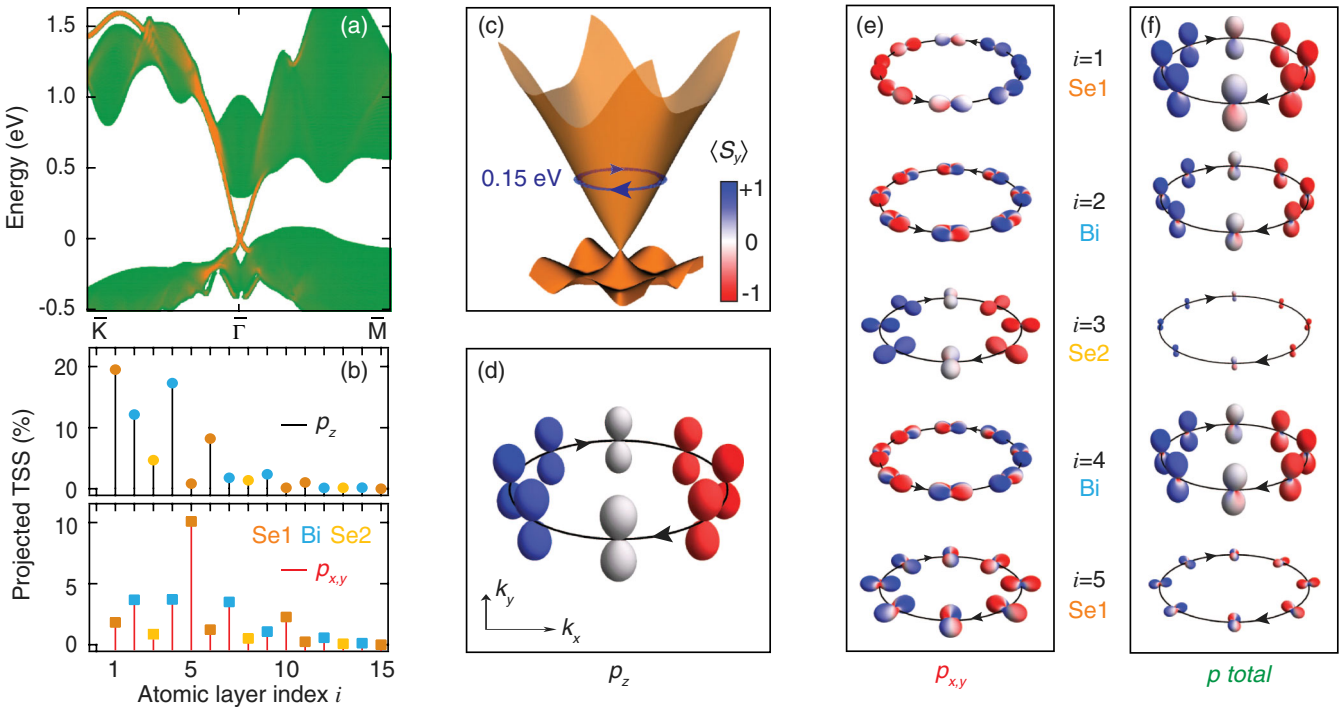

FIG. 3 (color online). (a) Electronic dispersion from our 250-layer-slab DFT model [20], with TSS in orange and bulk states in green [34]. (b) Percentage contribution of p_z and $p_{x,y}$ orbitals to Ψ_{TSS} at 0.15 eV above the DP, resolved layer-by-layer, for the top 15 atomic layers. (d)–(f) Layer- and orbital-projected charge density along the 0.15 eV k-space contour indicated in (c); their surfaces are defined by $r(\theta, \phi) = \sum_{\tau,\tau'} Z_\tau(\theta, \phi) Z_{\tau'}(\theta, \phi) \langle a^\dagger_{i,\tau,k} a_{i,\tau',k} \rangle$, where i and τ are layer and orbital basis indexes and Z the cubic harmonics, and colored according to the expectation value of the S_y operator. The *total* layer-resolved TSS texture (f) is obtained by adding all p orbital contributions according to their relative, layer-dependent weight from panel (b).

conduction band [27]. As a final test of the robustness of our DFT analysis of Ψ_{TSS}, we have calculated constant-energy circular dichroism ARPES patterns, which are also in excellent agreement with previous studies [30,31].

To gain a microscopic understanding of the properties of Ψ_{TSS} we present our DFT results for a 250-layer slab of Bi_2Se_3 [20] in Fig. 3(a), with bulk states in green and TSS in orange. The in- and out-of-plane p orbital projections in Fig. 3(b) confirm that Ψ_{TSS} indeed has a large p_z (70%) character—although $p_{x,y}$ (30%) is also significant—and most importantly that Ψ_{TSS} extends deep into the solid. Even though the orbital weight decays exponentially with the distance from the surface, as expected for a surface bound-state, Ψ_{TSS} extends ~2 quintupole layers (QL) below the surface (~ 2 nm), with ~75% contribution from the 1st QL and ~25% from the 2nd QL. Note also the interesting layer dependence of the orbital character: while for most layers the main component is the out-of-plane p_z, for the 5th the in-plane $p_{x,y}$ is actually dominant.

As a consequence of the relativistic SOI, which directly connects orbitals to spin flips via the $l^{\pm}s^{\mp}$ terms of the spin-orbit operator $\mathbf{l} \cdot \mathbf{s} = l_z s_z + (l^+ s^- + l^- s^+)/2$, the strongly layer-dependent orbital occupation becomes entangled with the spin polarization of Ψ_{TSS}. To visualize this entanglement, in Figs. 3(d)–3(f) we present the layer- and orbital-projected charge density along the 0.15 eV Dirac contour indicated in Fig. 3(c), colored according to the expectation value of the S_y operator [20]. The p_z-projected charge density, being associated with a single orbital, cannot be entangled and has the layer-independent spin helicity shown in Fig. 3(d). In contrast, a strong layer-dependent spin-orbital entanglement is observed for $p_{x,y}$ because the eigenstates can be a linear combination of $p_{x,\uparrow}$, $p_{y,\downarrow}$, and similar states, resulting in a complex set of charge-density surfaces. These surfaces show two overall spatial configurations oriented tangentially and radially with respect to the Dirac contour, with opposite spin helicity, as seen in Fig. 3(e). In Fig. 3(f) we show the total layer-dependent charge density obtained by adding in- and out-of-plane contributions according to their relative weights in Fig. 3(b); from this it is clear that while the p_z orbitals dominate, the $p_{x,y}$ orbitals lead to a substantial spin-orbital entanglement of the combined Ψ_{TSS}.

This entanglement also leads to complex in- and out-of-plane spin texture, as shown in Figs. 4(a)–4(d) where the layer-integrated spin patterns of individual and total p orbitals are presented. While for p_z we find the in-plane helical spin texture expected for the TSS, this is not the case for the p_x and p_y orbitals, which exhibit patterns opposite to one another. Combining all contributions $[\langle \vec{S}^{\mathrm{total}} \rangle / n_{\mathrm{total}}$ in Fig. 4(d)], the TSS out-of-plane spin texture vanishes in the vicinity of the DP; most important, the in-plane spin polarization is reduced from 100% to 75% at

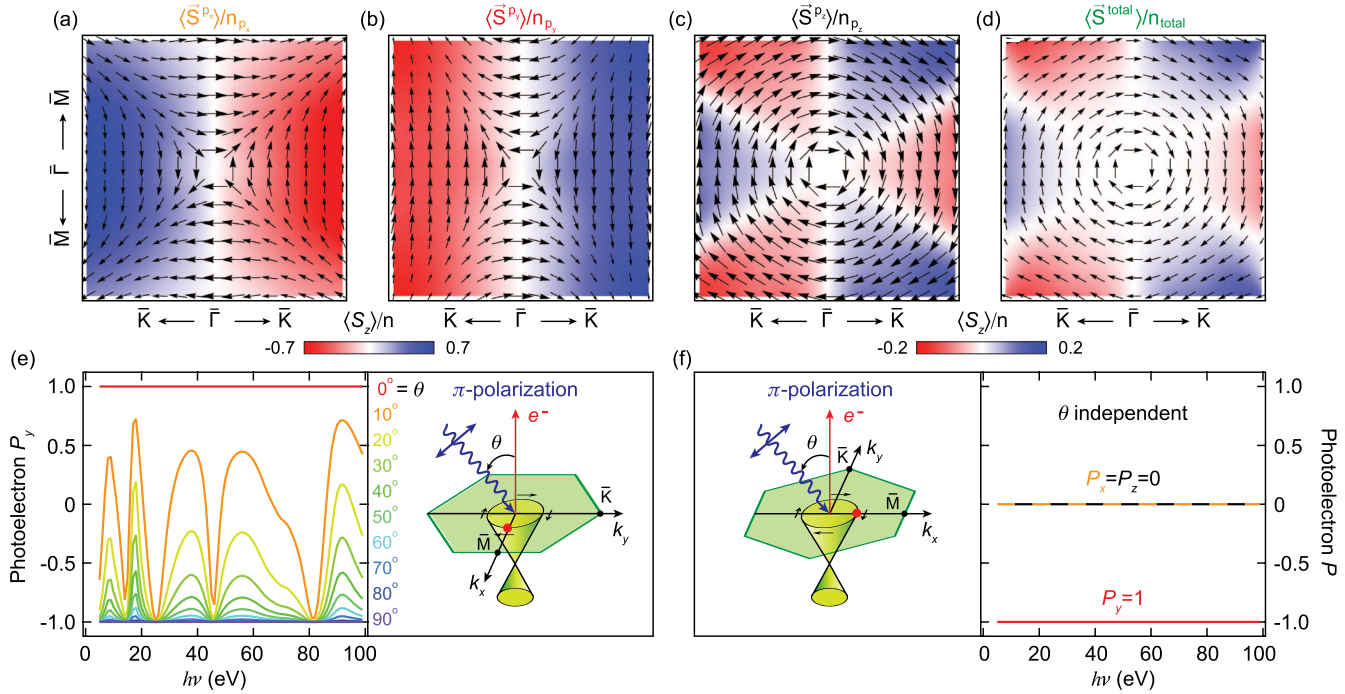

FIG. 4 (color online). (a)–(d) Spin texture of the Bi_2Se_3 Dirac cone upper branch (arrows: in-plane; colors: out-of-plane), obtained from the expectation value of the layer-integrated, orbital-projected spin operators, normalized to the orbital occupation [20]. Note that (a), (b) and (c), (d) have different color scales but that the arrow scaling is the same; also, moving away from $\bar{\Gamma}$ corresponds to moving in energy away from the DP (~ 0.4 eV at maps edge). (e), (f) Prediction for the photoelectron spin polarization (P) measured in spin-resolved ARPES as a function of photon energy and incidence angle [20]; two experimental geometries are examined in π polarization for the same k point located at 0.15 eV along $\bar{\Gamma} - \bar{M}$ [in (e) only P_y is shown].

the DP, and to 60% at 0.4 eV above the DP [20]. Note that this is also critically dependent on the relative $p_{x,y}$ orbital content of Ψ_{TSS}, which increases from 25% to 45% over the same energy range [20].

For the discussion of the ARPES intensity [20], we will here use the approximation $I \propto |\langle e^{i\mathbf{k}\cdot\mathbf{r}} | \mathbf{A}\cdot\mathbf{p} | \Psi_{\mathrm{TSS}} \rangle|^2$, expressed in terms of plane-wave photoelectron final states for simplicity. By writing Ψ_{TSS} as a linear combination of layer-dependent eigenstates, $\Psi_{\mathrm{TSS}} = \sum_{i,\sigma} \alpha_i \psi^{\sigma}_{i,\mathbf{k}_\parallel}$ with i and σ being layer and spin indexes, the ARPES intensity becomes $I \propto \sum_\sigma |\sum_i e^{-ik_z z_i} \langle e^{i\mathbf{k}_\parallel\cdot\mathbf{r}_\parallel} | \mathbf{A}\cdot\mathbf{p} | \alpha_i \psi^{\sigma}_{i,\mathbf{k}_\parallel} \rangle|^2$. Here, the $e^{-ik_z z_i}$ phase term accounts for the photoelectron optical path difference stemming from the TSS finite extent into the bulk. Because both $e^{-ik_z z_i}$ and $\psi^{\sigma}_{i,\mathbf{k}_\parallel}$ vary from layer to layer [the latter via the relative orbital content as shown in Fig. 3(f)], the photoemission intensity is dominated by interference between the $\psi^{\sigma}_{i,\mathbf{k}_\parallel}$ eigenstates, and can in fact be regarded as the Fourier transform of the layer-dependent Ψ_{TSS}. We also note that, because the phase of photoelectrons is defined by additive k_z and $\mathbf{k}_\parallel$ contributions, reversing the sign of either k_z or $\mathbf{k}_\parallel$ will change the ARPES intensity, i.e., $I(k_z) \neq I(-k_z)$ and especially $I(\mathbf{k}_\parallel) \neq I(-\mathbf{k}_\parallel)$ as observed experimentally.

Photoelectron interference also severely affects the spin polarization $P_{x,y,z} = (I^{\uparrow x,y,z} - I^{\downarrow x,y,z})/(I^{\uparrow x,y,z} + I^{\downarrow x,y,z})$ measured in spin-resolved ARPES [20]. This exhibits a strong dependence on photon energy, polarization, and angle of incidence, which in general prevents the straightforward experimental determination of the intrinsic spin-texture of Bi_2Se_3. While comprehensive results are presented in Figs. S2 and S3 [20], in Figs. 4(e) and 4(f) we show as an example the same k point along $\bar{\Gamma} - \bar{M}$ measured in two different geometries, probing selectively $p_{y,z}$ (e) and $p_{x,z}$ (f) orbitals. In Fig. 4(e), because $\langle \vec{S}^{p_y} \rangle$ and $\langle \vec{S}^{p_z} \rangle$ (the spin polarization of the p_y and p_z orbitals) are antiparallel at this specific k point, P_y varies between $\pm 100\%$ upon changing θ, and oscillates wildly as a function of photon energy (with the exception of 0° and 90°, which probe p_y and p_z separately). However, if the sample is rotated by 90° as in Fig. 4(f) $\langle \vec{S}^{p_x} \rangle$ becomes parallel to $\langle \vec{S}^{p_z} \rangle$ and the measured $P_{x,y,z}$ are all independent of photon energy and incidence angle, allowing the detection of the intrinsic spin polarization. We note that this behavior is consistent with reported spin-resolved ARPES results [16]: for the situation of Fig. 4(f), $P_y \gtrsim 80\%$ was obtained, close to our 100% expectation; along $\bar{\Gamma} - \bar{K}$, P_y was observed to vary from 25% at $h\nu = 36$ eV to -50% at 70 eV, while we obtain $+20 \pm 10\%$ and $-40 \pm 15\%$, respectively [20].

In conclusion, the TSS layer-dependent spin-orbital entanglement is responsible—via photoelectron interference—for the apparent time-reversal symmetry breaking in ARPES and the large discrepancy in the estimated TSS

spin polarization from spin-resolved ARPES. This is of critical importance for many applications and fundamental studies of TIs; e.g., the observed $I(\mathbf{k}_\parallel) \neq I(-\mathbf{k}_\parallel)$ provides an explanation for the so-far puzzling result of spin-polarized electrical currents photoinduced by linearly polarized light [32], which also is associated with an imbalance in the number of photoelectrons removed at $\pm\mathbf{k}_\parallel$. In addition, exploiting photoelectron interference in spin-resolved ARPES provides a way not only to probe the intrinsic spin texture of TIs, but also—and most importantly—to precisely control in- and out-of-plane spin polarization of the photocurrent in spin-resolved ARPES—all the way from 0 to $\pm 100\%$—by varying energy, polarization, and angle of incidence of the incoming photons.

We gratefully acknowledge M. Franz, G. A. Sawatzky, and H. Guo for discussions. This work was supported by the Max Planck—UBC Centre for Quantum Materials, the Killam, Alfred P. Sloan, Alexander von Humboldt, and NSERC's Steacie Fellowships (A. D.), the Canada Research Chairs Program (A. D.), NSERC, CFI, and CIFAR Quantum Materials. Work at the University of Maryland was supported by NSF-MRSEC (Grant No. DMR-0520471) and DARPA-MTO (Grant No. N66001-09-c-2067).

*damascelli@physics.ubc.ca

[1] C. L. Kane and E. J. Mele, Phys. Rev. Lett. **95**, 146802 (2005).
[2] B. A. Bernevig and S.-C. Zhang, Phys. Rev. Lett. **96**, 106802 (2006).
[3] L. Fu, C. L. Kane, and E. J. Mele, Phys. Rev. Lett. **98**, 106803 (2007).
[4] J. E. Moore and L. Balents, Phys. Rev. B **75**, 121306 (2007).
[5] X.-L. Qi, T. L. Hughes, and S.-C. Zhang, Phys. Rev. B **78**, 195424 (2008).
[6] M. Hasan and C. Kane, Rev. Mod. Phys. **82**, 3045 (2010).
[7] B. A. Bernevig, T. L. Hughes, and S.-C. Zhang, Science **314**, 1757 (2006).
[8] M. König, S. Wiedmann, C. Brone, A. Roth, H. Buhmann, L. W. Molenkamp, X.-L. Qi, and S.-C. Zhang, Science **318**, 766 (2007).
[9] H. Zhang, C.-X. Liu, X.-L. Qi, X. Dai, Z. Fang, and S.-C. Zhang, Nat. Phys. **5**, 438 (2009).
[10] Y. Xia, D. Qian, D. Hsieh, L. Wray, A. Pal, H. Lin, A. Bansil, D. Grauer, Y. S. Hor, R. J. Cava, and M. Z. Hasan, Nat. Phys. **5**, 398 (2009).
[11] Y. L. Chen, J. H. Chu, J. G. Analytis, Z. K. Liu, K. Igarashi, H. H. Kuo, X. L. Qi, S. K. Mo, R. G. Moore, D. H. Lu, M. Hashimoto, T. Sasagawa, S. C. Zhang, I. R. Fisher, Z. Hussain, and Z. X. Shen, Science **329**, 659 (2010).
[12] D. Hsieh, Y. Xia, D. Qian, L. Wray, J. H. Dil, F. Meier, J. Osterwalder, L. Patthey, J. G. Checkelsky, N. P. Ong, A. V. Fedorov, H. Lin, A. Bansil, D. Grauer, Y. S. Hor, R. J. Cava, and M. Z. Hasan, Nature (London) **460**, 1101 (2009).
[13] S. Souma, K. Kosaka, T. Sato, M. Komatsu, A. Takayama, T. Takahashi, M. Kriener, K. Segawa, and Y. Ando, Phys. Rev. Lett. **106**, 216803 (2011).
[14] S.-Y. Xu, Y. Xia, L. A. Wray, S. Jia, F. Meier, J. H. Dil, J. Osterwalder, B. Slomski, A. Bansil, H. Lin, R. J. Cava, and M. Z. Hasan, Science **332**, 560 (2011).
[15] Z.-H. Pan, E. Vescovo, A. V. Fedorov, D. Gardner, Y. S. Lee, S. Chu, G. D. Gu, and T. Valla, Phys. Rev. Lett. **106**, 257004 (2011).
[16] C. Jozwiak, Y. L. Chen, A. V. Fedorov, J. G. Analytis, C. R. Rotundu, A. K. Schmid, J. D. Denlinger, Y.-D. Chuang, D.-H. Lee, I. R. Fisher, R. J. Birgeneau, Z.-X. Shen, Z. Hussain, and A. Lanzara, Phys. Rev. B **84**, 165113 (2011).
[17] O. V. Yazyev, J. E. Moore, and S. G. Louie, Phys. Rev. Lett. **105**, 266806 (2010).
[18] Y. Zhao, Y. Hu, L. Liu, Y. Zhu, and H. Guo, Nano Lett. **11**, 2088 (2011).
[19] C.-H. Park and S. G. Louie, Phys. Rev. Lett. **109**, 097601 (2012).
[20] See Supplemental Material at http://link.aps.org/supplemental/10.1103/PhysRevLett.110.216401 for experimental details, and methods used to calculate the theoretical results in Figs. 2–4—inclusive of selection rules, Bi and Se cross sections, and photoelectron escape depth.
[21] Z.-H. Zhu, G. Levy, B. Ludbrook, C. N. Veenstra, J. A. Rosen, R. Comin, D. Wong, P. Dosanjh, A. Ubaldini, P. Syers, N. P. Butch, J. Paglione, I. S. Elfimov, and A. Damascelli, Phys. Rev. Lett. **107**, 186405 (2011).
[22] Y. Cao, J. A. Waugh, X.-W. Zhang, J.-W. Luo, Q. Wang, T. J. Reber, S. K. Mo, Z. Xu, A. Yang, J. Schneeloch, G. Gu, M. Brahlek, N. Bansal, S. Oh, A. Zunger, and D. S. Dessau, arXiv:1209.1016.
[23] M. Bianchi, D. Guan, S. Bao, J. Mi, B. B. Iversen, P. D. C. King, and P. Hofmann, Nat. Commun. **1**, 128 (2010).
[24] M. Lindroos, S. Sahrakorpi, and A. Bansil, Phys. Rev. B **65**, 054514 (2002).
[25] J. G. Checkelsky, Y. S. Hor, M.-H. Liu, D.-X. Qu, R. J. Cava, and N. P. Ong, Phys. Rev. Lett. **103**, 246601 (2009).
[26] Note that the threefold pattern is associated with the k_z dispersion of valence- and conduction-band bulk states.
[27] In the experiment, the bulk conduction band is significantly broadened by disorder-induced scattering, which leads to intensity leaking down to lower binding energies inside the gap, an effect not accounted for in our calculations. We also note that while this same disorder affects to some degree the linewidth and electronic filling of the TSS, its main features—such as dispersion and spin-orbital texture close to the Dirac point—are retained, as a manifestation of topological protection [28,29].
[28] P. Roushan, J. Seo, C. V. Parker, Y. S. Hor, D. Hsieh, D. Qian, A. Richardella, M. Z. Hasan, R. J. Cava, and A. Yazdani, Nature (London) **460**, 1106 (2009).
[29] Z. Alpichshev, J. G. Analytis, J.-H. Chu, I. R. Fisher, Y. L. Chen, Z. X. Shen, A. Fang, and A. Kapitulnik, Phys. Rev. Lett. **104**, 016401 (2010).
[30] Y. H. Wang, D. Hsieh, D. Pilon, L. Fu, D. R. Gardner, Y. S. Lee, and N. Gedik, Phys. Rev. Lett. **107**, 207602 (2011).
[31] S. R. Park, J. Han, C. Kim, Y. Y. Koh, C. Kim, H. Lee, H. J. Choi, J. H. Han, K. D. Lee, N. J. Hur, M. Arita, K. Shimada, H. Namatame, and M. Taniguchi, Phys. Rev. Lett. **108**, 046805 (2012).
[32] J. W. Mciver, D. Hsieh, H. Steinberg, P. Jarillo-Herrero, and N. Gedik, Nat. Nanotechnol. **7**, 96 (2011).
[33] Note that the TSS calculations have actually been performed for 0.12 and 0.2 eV, in order to account for the DP-conduction-band gap renormalization observed between experiment ($\sim$ 26 meV) and DFT (300 meV).
[34] Ψ_{TSS} is composed of those states that exceed a 20% projection onto the top 5 atomic layers in real space.

Supplemental materials for
Layer-by-layer entangled spin-orbital texture of the topological surface state in Bi_2Se_3

Z.-H. Zhu, C.N. Veenstra, G. Levy, A. Ubaldini, P. Syers, N.P. Butch,
J. Paglione, M.W. Haverkort, I.S. Elfimov, A. Damascelli,*

SM A. Materials and methods

ARPES experiments:

Angle-resolved photoemission spectroscopy (ARPES) was performed at UBC using a SPECS Phoibos 150 hemispherical analyzer and a monochromatized and linearly polarized UVS300 gas-discharge lamp. Energy and angular resolutions were set to 10 meV and $\pm 0.1^\circ$. We used 21.2 eV photons, whose close-to-100% linear polarization can be rotated to any arbitrary angle without changing sample orientation; in this study we focused on experiments for horizontal (π) and vertical (σ) polarizations. Bi_2Se_3 single crystals were grown from the melt at the University of Maryland [with carrier density $n \simeq 1.24{\times}10^{19}$ cm^{-3} (*1*)], and by floating zone at the University of Geneva. The samples were prealigned ex situ by conventional Laue diffraction, and cleaved and measured at pressures better than 5×10^{-11} torr and at a constant temperature of 6 K (*2*).

Density functional theory model for ARPES intensity calculations:

The bulk electronic structure of Bi_2Se_3 was calculated using the tight-binding order-N muffin-tin orbital (TB-NMTO) (*3,4*) and full-potential WIEN2k (*5*) density functional theory codes; we find excellent agreement between the two methods. The TB-NMTO approach is used to down-fold the *ab-initio* Hamiltonian to a 15-band model involving only the p orbitals of Bi and Se. This allows us to extract on-site energies and hopping parameters which are used to construct a 250-layer thick slab TB model (i.e., 50 quintupole layers), with atomic spin-orbit interaction (SOI) included as a local term for Bi and Se orbitals [1.25 eV and 0.22 eV, respectively (*6*)]. The chemical potential of this electronic structure is shifted to match that experimentally observed (we note that the TSS itself is topologically protected from local disorder, including that from the potential defects and vacancies which may cause such a doping). To understand the microscopic origin of the ARPES intensity patterns in Fig. 1 of the main text, we have performed photoemission intensity calculations for both linearly and circularly polarized light. Following an established approach (*7*), photoelectron final states are treated as spin-degenerate plane waves; however, to account for ARPES matrix elements, these plane waves have been expanded in spherical harmonics and Bessel functions around each atom. Since the initial states have mainly p orbital character, conservation of angular momentum only allows excitations into s and d-like free-electron states. Under these selection rules, photoelectrons from p_x, p_y, and p_z orbitals can be excited by x, y, and z polarized light respectively (*8*); all other excitations are forbidden. Finally, the Bi and Se atomic cross sections [e.g., 2.7 for Bi $6p$ and 8.0 for Se $4p$ at photon energy 21.2 eV (*9*)] also have been taken into account in calculating photoemission intensities, as well as the finite escape depth of the photoelectrons. Also note that throughout the paper, the coordinate system is consistent with the crystal structure: the k_x axis is along $\bar{\Gamma}-\bar{\mathrm{M}}$, the k_y axis is along $\bar{\Gamma}-\bar{\mathrm{K}}$, and the z axis is along the sample normal [001].

SM B. ARPES intensity and interference effects

In the following sections we will show how we calculated the data presented in the main text. We will begin, in this section, by calculating the explicit ARPES intensity based on our *ab-initio* TB model. In the following section, SI C, we will calculate the spin-polarization of photoelectrons, and how that relates to the TSS ground-state spin-polarization; importantly we will note how they can differ due to interference terms, and also depend on the relative orbital occupations. In SI D we will present these relative orbital occupations, while in SI E we resolve the interference terms and explicitly present the spin texture patters of photoelectrons for some example experimental configurations.

Based on Fermi's golden rule, the photoemission intensity can be written as (*7, 8*):

$$I \propto |\langle \Psi_f | \mathbf{A} \cdot \mathbf{p} | \Psi_i \rangle|^2, \tag{1}$$

where $\mathbf{p}$ is the electron momentum operator, $\mathbf{A}$ the electromagnetic vector potential, and Ψ_i and Ψ_f the initial- and final-state wavefunctions. We use the dipole approximation in the calculations such that $\mathbf{A} \cdot \mathbf{p}$ is approximated by $\mathbf{r}$. Here we focus on the photoemission of the topological surface states (TSS). Therefore, $\Psi_i = \Psi_{\mathrm{TSS}}$ which is the wavefunction of the TSS and can be written as a linear combination of atomic wavefunction in our *ab-initio* TB model:

$$\Psi_{\mathrm{TSS}} = \sum_{i,\tau,\sigma} C^{\sigma}_{i,\tau} \psi_{i,\tau}. \tag{2}$$

Here i is the atomic layer index along the z axis of the slab with the surface layer at $i = 1$, the orbital basis is given by $\tau \in \{p_x, p_y, p_z\}$, σ is the spin index which is $\uparrow$ or $\downarrow$, and $\psi_{i,\tau}$ are the atomic wavefunctions of orbital τ centered around the atomic layer i. The photoelectron final states are treated as free-electron-like, whose wavefunction can be described by a plane wave $\Psi_f = e^{\mathrm{i}\mathbf{k}\cdot\mathbf{r}}$. We can therefore define the matrix element term as:

$$M_{i,\tau} \equiv \langle e^{\mathrm{i}\mathbf{k}\cdot\mathbf{r}} | \mathbf{A} \cdot \mathbf{p} | \psi_{i,\tau} \rangle. \tag{3}$$

As discussed in the main text, the TSS is not a perfect two-dimensional state with a delta-function-like density in the z direction. Instead, it extends more than 2 nm deep into the bulk along the z direction. We take into account the spatial extent of the wavefunction along z by assigning an atomic-layer-dependent phase to photoelectrons: $e^{\mathrm{i}k_z z_i}$, with z_i being the position of the atomic layer i along z and $k_z = \sqrt{\frac{2m_e}{\hbar^2}(h\nu - E_B) - k_x^2 - k_y^2}$ is the momentum of photoelectrons along z, which depends on photon energy $h\nu$ and the initial-state binding energy E_B. Note that the phase of the photoelectrons is determined by their kinetic energy inside the material rather than in the vacuum; for this reason we do not consider the work function here. The finite photoelectron escape depth is also considered in our calculation, by including an exponential attenuation factor dependent on the mean free path (λ) of the photoexcited electrons; we used $\lambda = 7\,\text{Å}$, although no substantial change in our results was observed in the $5 - 10\,\text{Å}$ range. In order to show the effects of photon energy and escape depth, we redefine Eq. 3 as:

$$M_{i,\tau} \equiv e^{-\mathrm{i}k_z z_i} e^{-z_i/(2\lambda)} \langle e^{\mathrm{i}\mathbf{k}_\parallel \cdot \mathbf{r}_\parallel} | \mathbf{A} \cdot \mathbf{p} | \psi_{i,\tau} \rangle. \tag{4}$$

with $\mathbf{k} = \{k_x, k_y, k_z\}$ and $\mathbf{k}_\parallel = \{k_x, k_y\}$. Finally, Eq. 1 can be written as the sum of the intensity from up and down spin channels:

$$I \propto \sum_{\sigma=\uparrow,\downarrow} |\sum_{i,\tau} C_{i,\tau}^{\sigma} M_{i,\tau}|^2. \tag{5}$$

The latter we can expanded to obtain the explicit form of the ARPES intensity:

$$I = \sum_{i,\tau} ({C_{i,\tau}^{\uparrow}}^* C_{i,\tau}^{\uparrow} + {C_{i,\tau}^{\downarrow}}^* C_{i,\tau}^{\downarrow}) |M_{i,\tau}|^2 + \sum_{i \neq i', \tau \neq \tau'} ({C_{i,\tau}^{\uparrow}}^* C_{i',\tau'}^{\uparrow} + {C_{i,\tau}^{\downarrow}}^* C_{i',\tau'}^{\downarrow}) M_{i,\tau}^* M_{i',\tau'}. \tag{6}$$

Here $\sum_{i,\tau} {C_{i,\tau}^{\uparrow}}^* C_{i,\tau}^{\uparrow} + {C_{i,\tau}^{\downarrow}}^* C_{i,\tau}^{\downarrow} = 1$ for the normalized TSS wavefunction and the sum $\sum_{i \neq i', \tau \neq \tau'}$ represents the interference between different terms in the basis set – i.e., orbitals in the same or different atomic layers.

SM C. Photoelectron spin polarization in spin-resolved ARPES

There is a clear analytical relationship between the photoelectron spin polarization measured by spin-resolved ARPES and the TSS ground-state spin polarization obtained from the expectation value of spin operators applied on the TSS wavefunction. In a simple system with a single orbital and a single atomic layer, the photoelectron spin polarization is given by the TSS ground-state spin polarization. For a system with multiple orbitals and atomic layers, the interference terms become important and lead to a deviation from the single-orbital and single-atomic-layer system. In the following part of this section, we will derive the relationship in the multi-orbital and -atomic layer system with the interference term included.

Spin-resolved ARPES measures the spin polarization along different quantization axes, which here are the x , y and z directions as defined in Fig. 1(a) of the main text. The photoelectron spin polarization vector (P) is defined as $P = [P_x, P_y, P_z]$ where:

$$P_{x,y,z} = \frac{I^{\uparrow_{x,y,z}} - I^{\downarrow_{x,y,z}}}{I^{\uparrow_{x,y,z}} + I^{\downarrow_{x,y,z}}}. \tag{7}$$

Hereafter, we define $\uparrow$ ($\downarrow$) $\equiv\uparrow_z$ ($\downarrow_z$) and use the usual spin relations:

$$\begin{aligned} |\uparrow\rangle &= \frac{1}{\sqrt{2}}(|\uparrow_x\rangle + |\downarrow_x\rangle) = \frac{1}{\sqrt{2}}(|\uparrow_y\rangle + |\downarrow_y\rangle), \\ |\downarrow\rangle &= \frac{1}{\sqrt{2}}(|\uparrow_x\rangle - |\downarrow_x\rangle) = \frac{1}{\sqrt{2}}(-\mathrm{i}|\uparrow_y\rangle + \mathrm{i}|\downarrow_y\rangle). \end{aligned} \tag{8}$$

By using Eq. 5, 7 and 8, we can calculate $P_{x,y,z}$:

$$\begin{aligned} P_x &= \frac{\sum_{i,\tau}({C^{\uparrow}_{i,\tau}}^* C^{\downarrow}_{i,\tau} + {C^{\downarrow}_{i,\tau}}^* C^{\uparrow}_{i,\tau})|M_{i,\tau}|^2 + \sum_{i\neq i',\tau\neq\tau'}({C^{\uparrow}_{i,\tau}}^* C^{\downarrow}_{i',\tau'} + {C^{\downarrow}_{i,\tau}}^* C^{\uparrow}_{i',\tau'})M^*_{i,\tau}M_{i',\tau'}}{I}, \\ P_y &= \frac{\sum_{i,\tau}\mathrm{i}(-{C^{\uparrow}_{i,\tau}}^* C^{\downarrow}_{i,\tau} + {C^{\downarrow}_{i,\tau}}^* C^{\uparrow}_{i,\tau})|M_{i,\tau}|^2 + \sum_{i\neq i',\tau\neq\tau'}\mathrm{i}(-{C^{\uparrow}_{i,\tau}}^* C^{\downarrow}_{i',\tau'} + {C^{\downarrow}_{i,\tau}}^* C^{\uparrow}_{i',\tau'})M^*_{i,\tau}M_{i',\tau'}}{I}, \\ P_z &= \frac{\sum_{i,\tau}({C^{\uparrow}_{i,\tau}}^* C^{\uparrow}_{i,\tau} - {C^{\downarrow}_{i,\tau}}^* C^{\downarrow}_{i,\tau})|M_{i,\tau}|^2 + \sum_{i\neq i',\tau\neq\tau'}({C^{\uparrow}_{i,\tau}}^* C^{\uparrow}_{i',\tau'} - {C^{\downarrow}_{i,\tau}}^* C^{\downarrow}_{i',\tau'})M^*_{i,\tau}M_{i',\tau'}}{I}. \end{aligned} \tag{9}$$

In order to clarify the relationship between the photoelectron spin polarization (Eq. 9) and the TSS ground-state spin polarization, we can express the photoelectron spin polarization in terms of expectation value of spin operators, with the spin operator defined as:

$$S_{\eta}^{i,\tau;i^{'},\tau^{'}} = |\psi_{i,\tau}\rangle\langle\psi_{i^{'},\tau^{'}}|\sigma_{\eta}, \tag{10}$$

where $\eta \in \{x, y, z\}$ and $\sigma_{x,y,z}$ are the Pauli spin matrices. Using Eq. 2 and Eq. 10, one can write down the expression for the layer- and orbital-projected expectation value of spin operators:

$$\begin{aligned}
\langle S_{x}^{i,\tau;i^{'},\tau^{'}}\rangle &= {C_{i,\tau}^{\uparrow}}^{*} C_{i^{'},\tau^{'}}^{\downarrow} + {C_{i,\tau}^{\downarrow}}^{*} C_{i^{'},\tau^{'}}^{\uparrow}, \\
\langle S_{y}^{i,\tau;i^{'},\tau^{'}}\rangle &= \mathrm{i}(-{C_{i,\tau}^{\uparrow}}^{*} C_{i^{'},\tau^{'}}^{\downarrow} + {C_{i,\tau}^{\downarrow}}^{*} C_{i^{'},\tau^{'}}^{\uparrow}), \\
\langle S_{z}^{i,\tau;i^{'},\tau^{'}}\rangle &= {C_{i,\tau}^{\uparrow}}^{*} C_{i^{'},\tau^{'}}^{\uparrow} - {C_{i,\tau}^{\downarrow}}^{*} C_{i^{'},\tau^{'}}^{\downarrow}.
\end{aligned} \tag{11}$$

The spin-polarization vector of the TSS ground state, defined as $\langle S^{\mathrm{TSS}}\rangle = [\langle S_x\rangle, \langle S_y\rangle, \langle S_z\rangle]$, is the sum of the expectation value of spin operators shown in Eq. 10 with $i = i^{'}$ and $\tau = \tau^{'}$: $\langle S_{\eta}^{\mathrm{TSS}}\rangle = \sum_{i,\tau}\langle S_{\eta}^{i,\tau}\rangle$. When $i \neq i^{'}$ and $\tau \neq \tau^{'}$, the spin operator in Eq. 10 represents the interference effect in the photoelectron spin polarization.

Plugging Eq. 11 into Eq. 9, we can now rewrite the photoelectron spin polarization in terms of the expectation values of spin operators as defined in Eq. 10:

$$P_{\eta} = \frac{\sum_{i,\tau}\langle S_{\eta}^{i,\tau}\rangle |M_{i,\tau}|^2 + \sum_{i\neq i^{'},\tau\neq\tau^{'}}\langle S_{\eta}^{i,\tau;i^{'},\tau^{'}}\rangle M_{i,\tau}^{*} M_{i^{'},\tau^{'}}}{I}. \tag{12}$$

This shows the relationship between the photoelectron and the TSS ground-state spin polarization. We can see that the matrix element $M_{i,\tau}$ and the interference term $\sum_{i\neq i^{'},\tau\neq\tau^{'}}$ can make the photoelectron spin polarization deviate from the TSS ground-state spin polarization.

SM D. TSS orbital character and spin polarization

As shown in Fig. 4 (a), (b) of the main text, p_x and p_y orbitals have almost opposite in-plane spin textures. Therefore, the in-plane spin polarization from the $p_{x,y}$ channel is almost zero

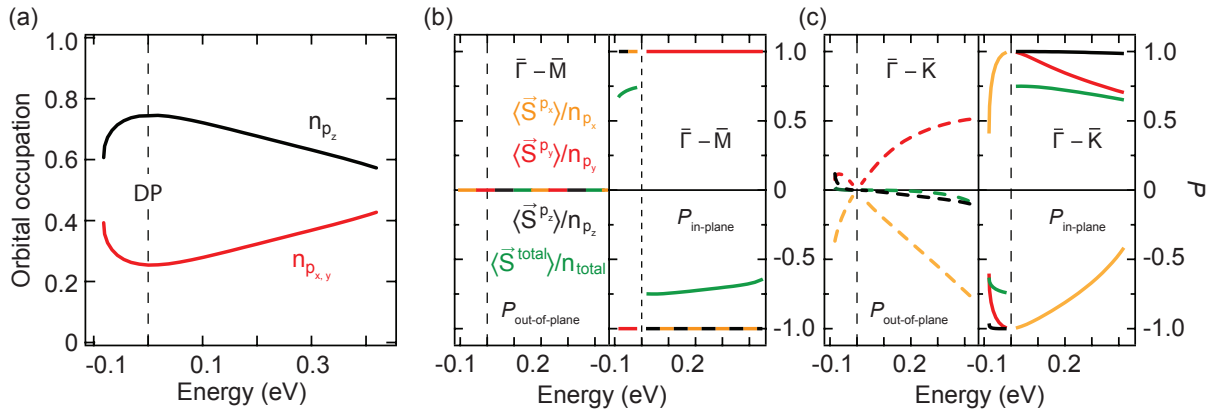

Fig. S1: (a) Energy dependence of the $p_{x,y}$ and p_z relative contributions to the TSS wavefunction. (b), (c) cuts through Fig. 4(a)-(d) from the main text showing the relative out-of-plane (left panel) and in-plane (right panel) spin polarization (P) of individual p orbitals as a function of energy along $\bar{\Gamma} \rightarrow \bar{\mathrm{M}}$ (b) and $\bar{\Gamma} \rightarrow \bar{\mathrm{K}}$ (c) [obtained from the expectation value of layer-integrated, orbital-projected spin operators, normalized to the orbital occupation shown in (a)].

over a large energy window, which results in a less than 100% TSS in-plane spin polarization. This orbital-dependent spin texture makes the relative occupation of $p_{x,y}$ and p_z critical to determine the value of the TSS in-plane spin polarization. Upon moving away from the Dirac point (DP), the $p_{x,y}$ occupation increases from 25% to 45% and the p_z occupation correspondingly decreases, as shown in Fig. S1(a). The in-plane and out-of-plane spin polarization of individual orbitals is shown in Fig. S1(b) (along $\bar{\Gamma} \rightarrow \bar{\mathrm{M}}$) and Fig. S1(c) ($\bar{\Gamma} \rightarrow \bar{\mathrm{K}}$). We can see that the TSS spin polarization for the total of p orbitals can never reach 100%; instead it decreases from 75 to $\sim 60\%$ while energy is increasing from 0 to 0.4 eV.

SM E. Photon energy-polarization dependence of ARPES spin texture

In Fig. 4(e) and (f) of the main text, we show that the photoelectron spin polarization can strongly depend on photon energy and experimental geometry. Here, in Fig. S2, we explicitly present the spin texture patterns of photoelectrons as measured by spin-resolved ARPES for different photon energies and polarizations . The strong deviations between photoelectron and

TSS ground-state spin textures can be seen by comparing Fig. S2(b)-(d) to Fig. 4(a)-(d) in the main text. One can also observe a remarkably strong and nontrivial photon energy dependence for the experimentally determined spin texture of photoelectrons. The only exception is the result obtained with π-polarization at a 90° incidence angle [Fig. S2(a)]: in this case one only probes initial states with p_z orbital character, whose spin texture is nearly layer-independent.

In Fig. S3, we focus on the photoelectron spin polarization vector at two **k** points under two experimental geometries, as a function of photon energy and incidence angle of π-polarized light. The photoelectrons excited under different experimental geometries are composed of electrons with different spin orientations, depending on their orbital source. Even at the same **k** point, the photoelectron spin polarization will change if we change the experimental geometry, as it can be seen by comparing Fig. S3(a) to S3(c) or Fig. S3(b) to S3(d). Moreover, the photoelectron spin polarization can be non-zero along directions which are expected to be zero based on the spin polarization of the TSS ground state. For instance, P_y and P_z in Fig. S3(a), P_x and P_z in Fig. S3(b), P_y and P_z in Fig. S3(c) are expected to be zero from the spin polarization of the TSS ground state; however, the photoelectron spin polarization of these components is not zero and has a very strong photon energy dependence as a result of interference effects between photoelectrons from different orbitals. Only the photoelectron spin polarization shown in Fig. S3(d) directly presents the TSS ground-state spin polarization owing to the fact that – thanks to the choice of geometry and light polarization – all photoelectrons from different layers and selected orbitals have the ground states with the same expectation value of spin operators; this eliminates possible deviations induced by matrix element and interference effects.

Note that our calculated spin polarization of photoelectrons is in quantitative agreement with reported spin-resolved ARPES results (*10*). For the situation shown in Fig. S3(c) and (d) along $\bar{\Gamma}-\bar{\mathrm{M}}$, $P_y \geq 80\%$ was reported, close to 100% obtained from the calculation; along $\bar{\Gamma}-\bar{\mathrm{K}}$, P_y was reported to be 25% at $h\nu$ = 36 eV and -50% at $h\nu$=70 eV at $k_y = \pm 0.11 \text{Å}^{-1}$, while our

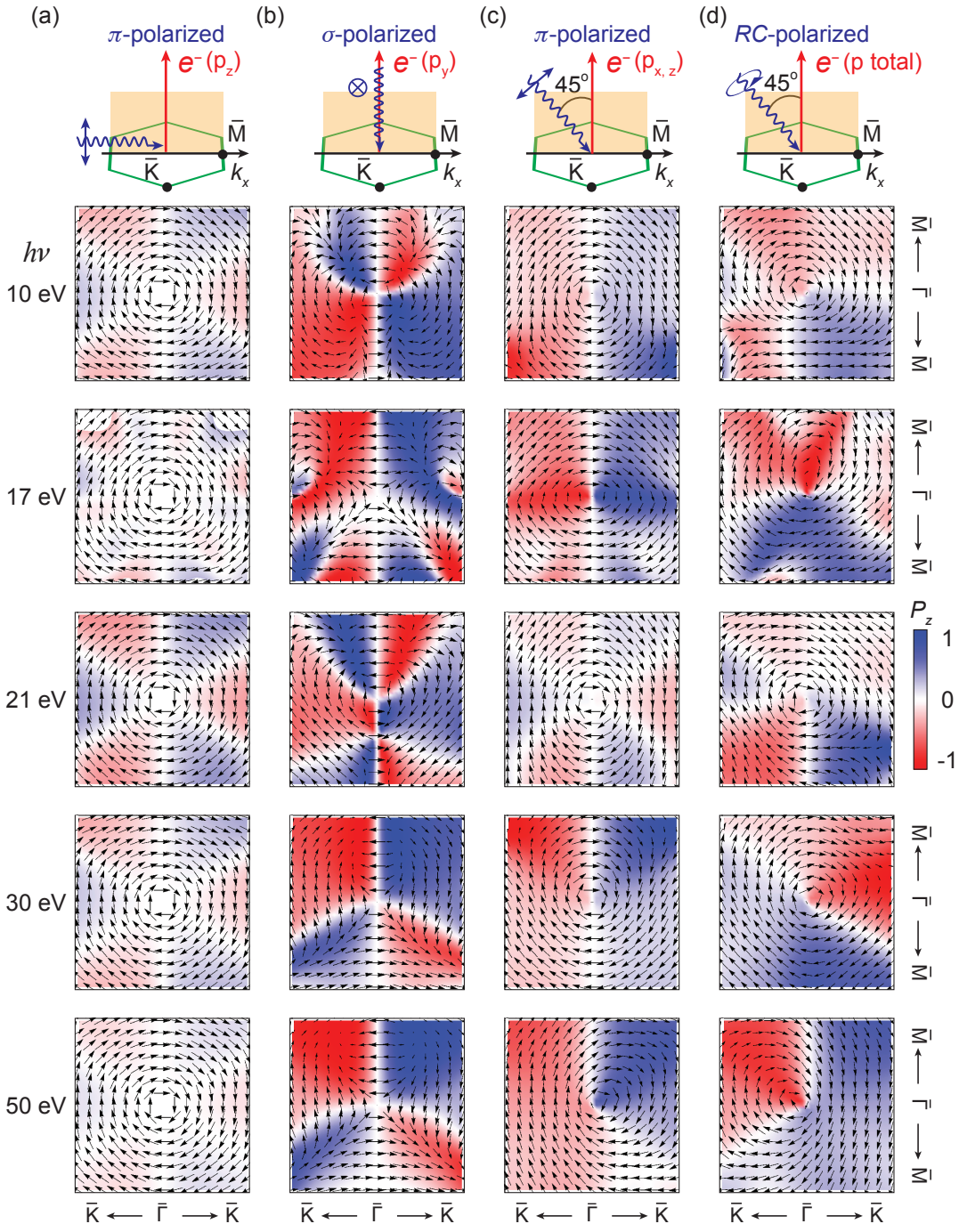

Fig. S2: Calculated spin textures of photoelectrons excited from the Dirac cone upper branch in Bi_2Se_3, for different photon energies and polarizations. Arrows and colors describe the in-plane and out-of-plane photoelectron spin polarization, respectively; note that moving away from the $\bar{\Gamma}$ point in these maps corresponds to moving along the Dirac dispersion away from the DP.

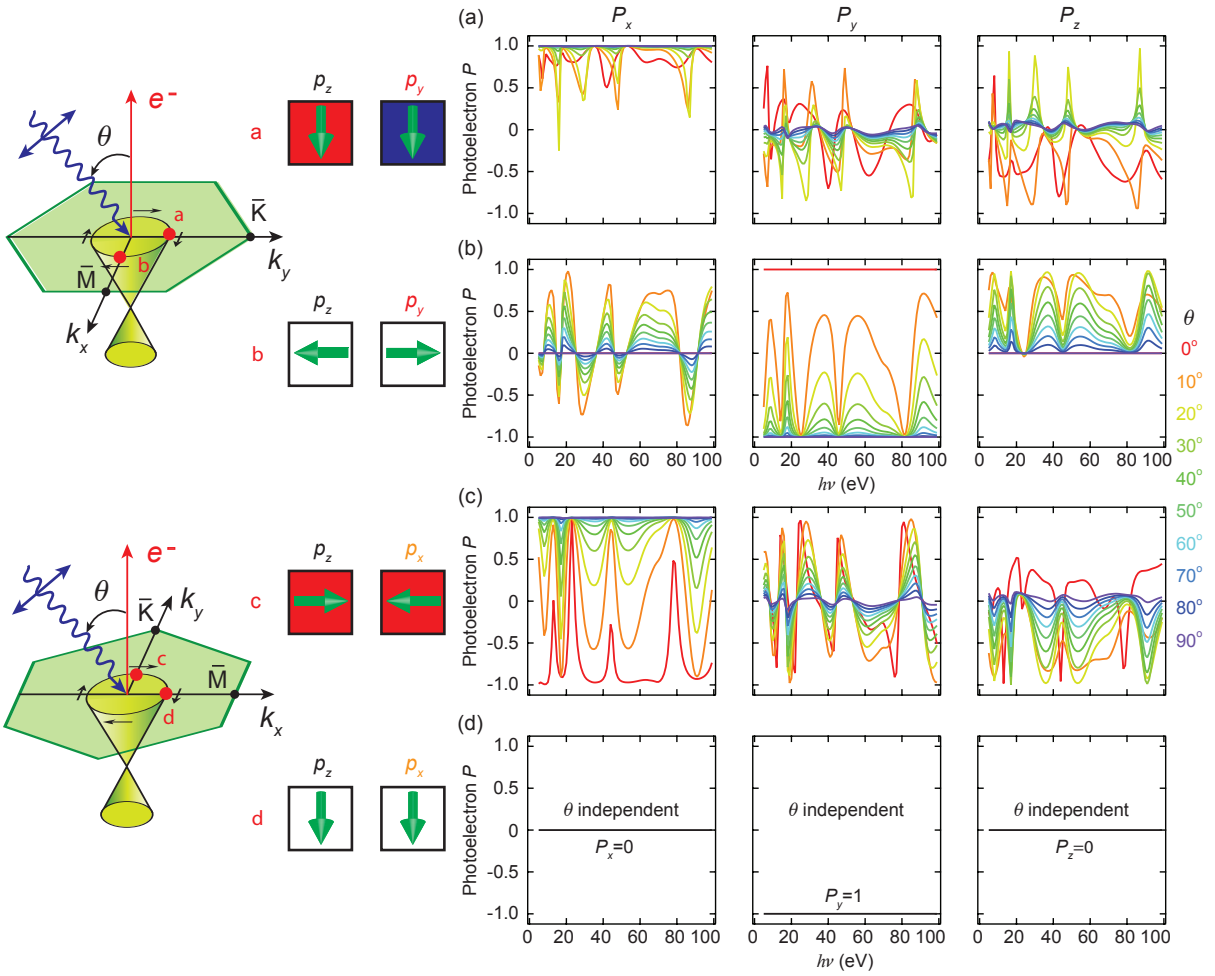

Fig. S3: Photon energy dependence of the photoelectron spin polarization. (a), (b) Calculated photoelectron spin polarization along x, y and z at two **k** points as a function of photon energy. The two measured **k** points are labeled by red dots in the schematics of experimental geometries shown on the left-hand side. The middle panels with green arrows and blue/red/white squares are used to schematically present the in-plane (green arrows) and out-of-plane (filled color with red: -; white: 0; blue: +) spin polarization of the only two atomic orbitals which emit photoelectrons based on selection rules. The right-hand-side three panels show the three components of the photoelectron spin polarization as a function of photon energy, with different incidence angles (θ) of the π-polarized light shown with color. (c), (d) Same data as in (a) and (b) but for a different experimental geometry as shown in the bottom left panel.

calculation gives $20\% \pm 10\%$ and $-40\% \pm 15\%$, respectively. The uncertainty of our results is estimated mainly based on the uncertain ratio between $p - to - s$ and $p - to - d$ excitations.

References

1. N. P. Butch, *et al.*, *Phys. Rev. B* **81**, 241301 (2010).

2. Z.-H. Zhu, *et al.*, *Phys. Rev. Lett.* **107**, 186405 (2011).

3. O. K. Andersen, *Phys. Rev. B* **12**, 3060 (1975).

4. O. K. Andersen, T. Saha-Dasgupta, *Phys. Rev. B* **62**, 16219 (2000).

5. P. Blaha, K. Schwarz, G. Madsen, D. Kvasnicka, J. Luitz, *An augmented plane wave plus local orbitals program for calculating crystal roperties* (Technical University of Wien, Vienna, 2001).

6. K. Wittel, R. Manne, *Theor. Chim. Acta.* **33**, 347 (1974).

7. M. Lindroos, S. Sahrakorpi, A. Bansil, *Phys. Rev. B* **65**, 054514 (2002).

8. A. Damascelli, *Physica Scripta* **T109**, 61 (2004).

9. J. J. Yeh, I. Lindau, *Atomic Data and Nuclear Data Tables* **32**, 1 (1985).

10. C. Jozwiak, *et al.*, *Phys. Rev. B* **84**, 165113 (2011).